Aspects on early-stage corrosion of different zinc alloys: wet $scCO_2$-induced corrosion

Ville Saarimaa[1+], Aaretti Kaleva[++], Erkki Levänen[++], Pasi Väisänen[+++], Antti Markkula[+++]

1 Corresponding author. Tel.: +358 44 099 6335. E-mail address: ville.saarimaa@topanalytica.com

[+]Top Analytica, Ruukinkatu 4, FI-20540 Turku, Finland

[++]Material Science and Environmental Engineering, Tampere University, FI-33101 Tampere, Finland

[+++]SSAB Europe, Harvialantie 420, FI-13300 Hämeenlinna, Finland

ABSTRACT

The surface activity of different zinc alloys was evaluated in wet $scCO_2$. The zinc coating surface chemistry governed the corrosion product formation. On zinc and Zn-Al coatings, the Al_2O_3 layer prevented growth of corrosion products. A Zn-Al-Mg coating showed high initial reactivity due to active Zn-Mg phases. An electrogalvanized coating was very active due to a high ratio of exposed, less dense planes. In a Zn-Fe coating, several Zn-Fe phases were susceptible to wet $scCO_2$ at the same time, triggering the sacrificial effect of Zn. Wet $scCO_2$ is a convenient medium to assess the early-stage corrosion of metal coatings.

Keywords: zinc, magnesium, aluminum, iron, (electro)galvanizing, $scCO_2$, corrosion

1 INTRODUCTION

The most economical way of protecting steel against corrosion is to coat it with zinc[1]. Over the past decades, a variety of galvanized alloys have been developed to meet the requirements of different end uses[2]. Standard hot dip galvanized zinc coating (Z) has good formability and corrosion resistance and is abundantly used in the construction industry and household appliances. Galfan (ZA) coating is composed of 5% Al and 95% Zn, and has a lamellar microstructure, which improves formability and corrosion resistance compared to the standard zinc coating[3–6]. An electrogalvanized (EZ) coating is composed of pure zinc. It is produced not by hot dipping, but in electroplating cells. This coating deposition mechanism produces a smooth surface and a coating with good formability and corrosion resistance. The EZ coatings are typically used in applications with very high demand for surface quality, such as automotive exterior panels. Galvanneal (ZF) coatings are zinc-iron coatings that possess superior welding properties and paint adhesion, and are utilized for example in automotive bodyworks[7,8]. ZF coatings are produced by heat treatment after the hot dipping process[9], and have higher hardness than normal Z coatings, but it also means somewhat impaired formability. Zinc-aluminum-magnesium (ZMA) alloys are the latest developments within the field of hot dip galvanizing[10]. ZMA coatings are claimed to possess higher corrosion resistance than the conventional zinc coating[11], which makes them lucrative replacements to zinc coatings in end uses where cost, material savings (thinner coatings) or better corrosion resistance is pursued. The long-term electrochemical activity is reportedly much lower for Mg-and Al-containing alloys compared to pure zinc coatings because of Mg^{2+} and Al^{3+} -induced quenching of corrosion activity[3,12]. Corrosion

resistance of different zinc alloys, with or without organic coatings, has been widely investigated during the past decades in studies comprehending atmospheric and accelerated exposures[1,8,13–26]. Corrosion of steel in CO_2 capture plants and natural gas pipelines has been thoroughly investigated[27]. Zinc is considered more corrosion resistant than steel in most natural atmospheres[1], but systematic studies of corrosion resistance of zinc alloys in wet supercritical carbon dioxide atmosphere (simulating corrosion in CO_2 capture pipelines) have not been carried out yet.

Atmospheric corrosion of zinc is an electrochemical process, initiated as anodic dissolution of zinc, balanced by oxygen reduction and/or hydrogen evolution at cathodic sites, and formation of zinc (oxy) hydroxide[1,12] (1-3).

$$Zn + 2OH^- \rightarrow Zn(OH)^2 + 2e^- \quad (1)$$

$$O_2 + 2H_2O + 4e^- \rightarrow 4OH^- \quad (2)$$

$$2H^+ + 2e^- \rightarrow H_2 \quad (3)$$

$Zn(OH)_2$ can dehydrate to ZnO and react with carbon dioxide dissolved in water (derived from carbon dioxide in the atmosphere), leading to a mixture of these compounds in the precipitated corrosion product layer[1] (4-6).

$$Zn(OH)_2 \rightarrow ZnO + H_2O \quad (4)$$

$$5Zn(OH)_2 + CO_2 \rightarrow 2ZnCO_3 \cdot 3Zn(OH)_2 + 2H_2O \quad (5)$$

$$5ZnO + 2CO_2 + 2H_2O \rightarrow 2ZnCO_3 \cdot 3Zn(OH)_2 \quad (6)$$

Formation of these less soluble zinc corrosion products, i.e. zinc patination, leads to passivation of the surface and decreased electrochemical activity. The formation of carbonates depends on the availability of CO_2 in the atmosphere and is accelerated at elevated CO_2 concentration[28]. In supercritical carbon dioxide, the CO_2 concentration is much higher than in the atmosphere. Nevertheless, wet $scCO_2$-induced corrosion is proposed to follow a similar reaction route than atmospheric corrosion[29]. The sole presence of CO_2 does not promote corrosion, but corrosion rates start to increase when water is available in the system, and when monolayers of water are absorbed on metal surface[30]. Dissolution of water into $scCO_2$ acidifies the system because of H_2CO_3 formation, which increases the corrosion rate of a metal. In wet $scCO_2$, at high water densities, electrochemical corrosion processes occur like in liquids with anodic and cathodic reactions (localized or delocalized) resulting in formation of soluble zinc cations and their precipitation[30]. The electrochemical reactions are depicted as follows[31]. Carbonic acid dissociates to carbonate and bicarbonate ions according to equations 7-9:

$$CO_2\,(g) + H_2O\,(l) \rightarrow H_2CO_3\,(aq) \quad (7)$$

$$H_2CO_3\,(aq) \rightarrow HCO_3^-\,(aq) + H^+\,(aq) \quad (8)$$

$$HCO_3^-\,(aq) \rightarrow CO_3^{2-}\,(aq) + H^+\,(aq) \quad (9)$$

Dissolved zinc ions and simple zinc corrosion products (equations 1 and 4) react with the carbonate ions, forming more complex and stable precipitates (10-12):

$$Zn^{2+}(aq) + CO_3^{2-}(aq) \rightarrow ZnCO_3(s) \quad (10)$$

$$aZn^{2+}(aq) + bCO_3^{2-}(aq) + cOH^-(aq) \rightarrow Zn_a(CO_3)_b(OH)_c(s) \quad (11)$$

$$Zn(OH)^+(aq) + HCO_3^-(aq) \rightarrow ZnCO_3(s) + H_2O(l) \quad (12)$$

The durability of a zinc coating is governed by the dissolution rate of zinc, and the best strategy for corrosion protection is to select a material resistant to corrosion in prevailing conditions[30]. Surface chemistry, morphology, alloying elements, phase composition and deposition process affect the corrosion resistance[18]. In this study, modern surface analytical tools are employed to assess the surface composition of different zinc alloys before and after wet $scCO_2$ exposure, and the effect of surface chemistry on early-stage wet $scCO_2$-induced corrosion is discussed.

2 EXPERIMENTAL PROCEDURES

2.1 Materials

The samples were obtained from SSAB Europe, and they are specified in Table 1.

2.2 Cleaning of panels

2.2.1 Solvent cleaning

The samples were wiped with water, acetone and isopropanol to produce the solvent cleaned specimens.

2.2.2 Alkaline cleaning

The alkaline cleaning bath contained 16 g of Gardoclean 338 (Chemetall) dissolved in 2 L deionized water. The free alkalinity was 8-9 meq/L. The cleaning procedure comprised dipping of panels in the cleaning bath and subsequent two-stage deionized water spray rinsing. The procedure was repeated two times. The temperature of the baths and the rinsing water was 60°C and the panels were exposed to each step for 4 s. Furnace drying at 60°C for 10 min concluded the cleaning procedure.

2.3 Wet $scCO_2$ exposure

Corrosion tests were done in a batch reactor pressurized with CO_2 gas. The treatments were carried out for specimens of 5x10 cm at 40°C and 100 bar for 60 min. The reaction conditions (40°C and 100 bar) were chosen based on previous studies at different pressures and temperatures, ranging from room temperature to 60°C and 80 bar to 300 bar[29,31,32]. At the chosen conditions, the exposures were successfully carried out in the supercritical region (without excessive pressure) with good repeatability. Parallel samples were exposed and analyzed. The amount of deionized water in the reactor was 5 mL. Details can be found in the paper by Kaleva et al.[33]

2.4 Quantification of corrosion products

The exposed samples were cured in a furnace (conversion of corrosion products to oxides), followed by step-wise extraction of the corrosion layer using a glycine/DI water solution (glycine ≥99%, Sigma-Aldrich, concentration 5 g/100 mL). Details of the extraction procedure can be found in previous publications [34,35]. Composition of the extracts was determined with XRF (Epsilon 3XL, PANalytical). Quantification was performed using a 50 kV voltage, a 109 μA current, a 180 s measurement time, and an Ag filter. Dissolved magnesium was measured with

inductively coupled plasma atomic emission spectroscopy (ICP-OES, Perkin Elmer Optima 5300 DV). Full solubility of corrosion products was confirmed by SEM imaging before and after extraction.

2.5 Surface analyses

Surface imaging and element mapping were done with a Zeiss Gemini 450 electron microscope equipped with a Bruker QUANTAX FlatQUAD EDS system. A 3 kV acceleration voltage was applied. Broad ion beam milling (Ilion+ Advantage Precision, Model 693, Gatan Inc., USA) was used for cross section preparation. Depth profiles were obtained with X-ray photoelectron spectroscopy (XPS, PHI Quantum 2000) using monochromated Al Kα beam and 100 µm spot size. The following lines were used for quantification: C1s, O1s, Al2p, Zn2p3, Mg2p and Fe2p3. C1s contamination on the outermost surface was omitted from the figures for clarity. For each sample, 3-9 depth profiles from different locations of the sample were analyzed to confirm the surface composition. Droplets of deionized water (1 µL volume) were placed on unexposed samples using an OCA 50 device (DataPhysics Instruments GmbH). The droplets were left to repose for 15 s, after which the static water contact angles were recorded. Surface roughness was determined using a confocal white light microscope (Nanofocus Msurf) with an Olympus 20x lens and an 80 µm cut-off. The roughness was expressed as the arithmetical mean height, Sa. A time-of-flight secondary ion mass spectrometer (ToF-SIMS, Phi Trift II) was employed for element mapping. The measurements were performed at 25 kV and 50 µm raster size. Fourier transform infrared spectroscopy was performed with a Bruker Alpha instrument at 2 cm^{-1} resolution. The measurements were performed in the region 375-4000 cm^{-1} with a single reflection diamond ATR.

3 RESULTS AND DISCUSSION

3.1 Characterization of samples prior to wet $scCO_2$ exposure

3.1.1 Chemical state

Solvent cleaning of metal substrates can remove surface contaminations, but does not affect the chemical surface composition of the metallic coating[36]. On the contrary, the alkaline cleaning step, which is employed in the beginning of most color coating lines to eliminate oil, dirt and lubricant residues, removes the outermost oxide layer and improves the reactivity of the surface[37]. This is illustrated in Figure 1, where the water contact angle shows lower values (better wettability and decreased surface hydrophobicity) after alkaline cleaning for all the studied substrates. The decrease in CA_{water} by alkaline cleaning was highest for the Z, ZA and ZF coatings, and lowest for ZMA and EZ coatings.

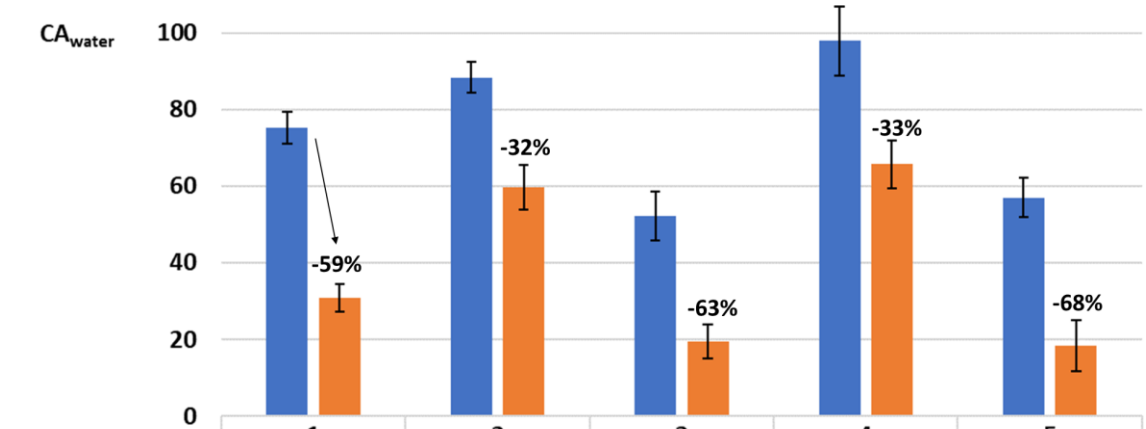

	1 Z	2 ZMA	3 ZA	4 EZ	5 ZF
Solvent cleaned	75	88	52	98	57
Alkaline cleaned	31	60	20	66	18

Figure 1. Water contact angles on different substrates after solvent cleaning and alkaline cleaning.

3.1.2 Roughness

Surface roughness results are shown in Figures 2 and 3. The samples Z and ZMA have comparable Sa values of about 0.4. Also, ZA and EZ have similar roughness (the Sa value was about 0.25). The surface roughness of Z, ZMA and ZA samples is derived from a similar large-scale skin passing pattern, while the roughness of the electrogalvanized coating (EZ) comes from the fine characteristic surface pattern[18]. The galvanneal coating showed the highest surface roughness, 0.77, which is a result of the post heat treatment that creates a very rough surface microstructure[8]. During the heat treatment after hot dip galvanizing process, the galvanneal coating loses its typical spangle appearance and roughness is remarkably increased[8]. A comparison between the surface roughness results and the water contact angle data (Fig. 1) shows that samples with similar surface roughness can have very different chemical states. This indicates that the surface chemistry has a more important role on the surface reactivity than the roughness[38].

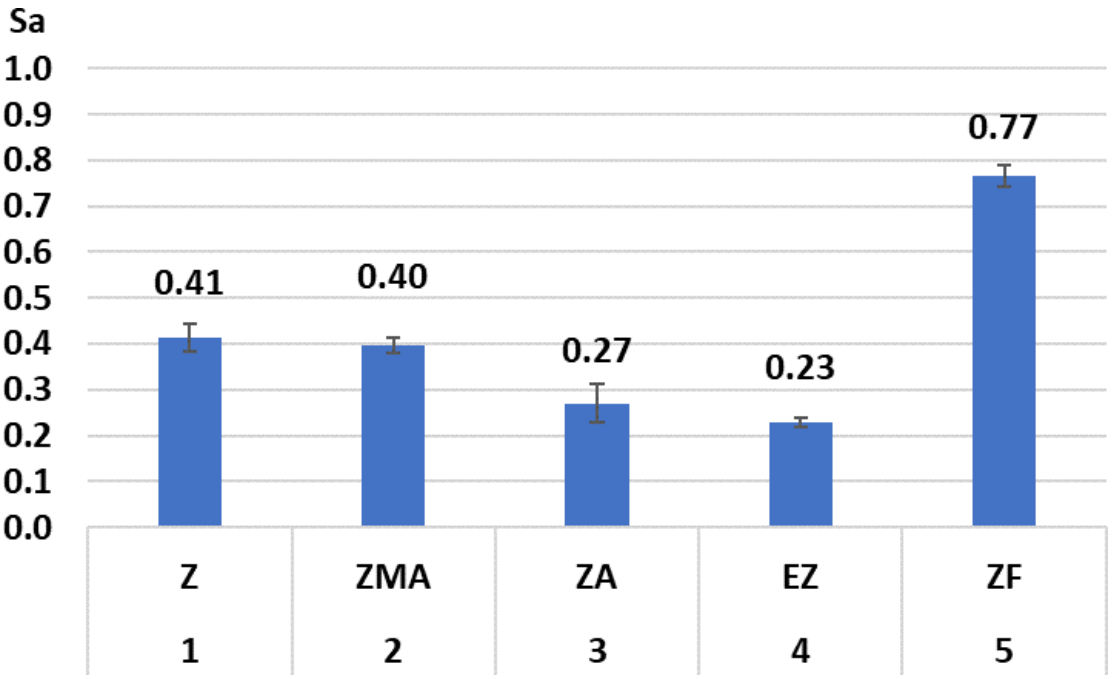

Figure 2. Roughness values of the studied substrates.

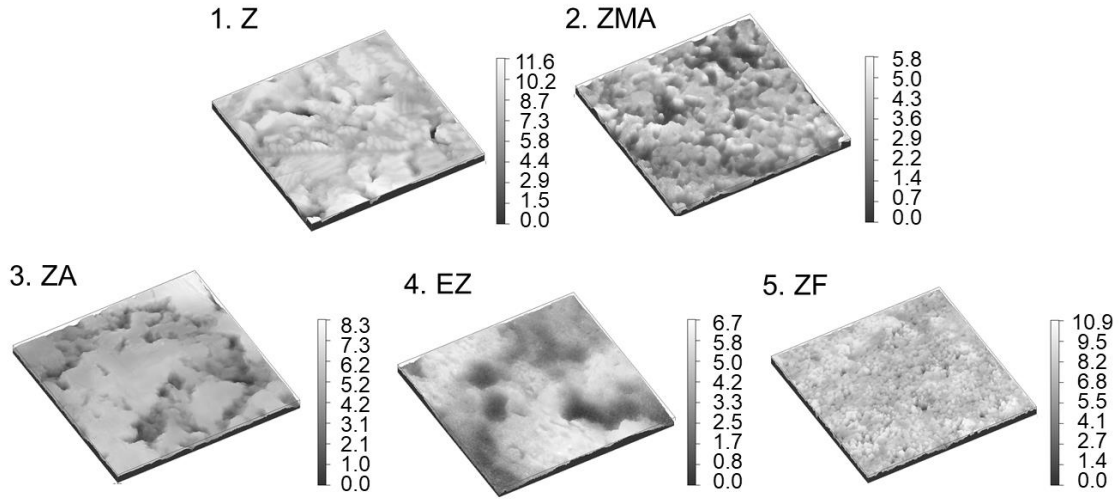

Figure 3. Confocal microscopy contour maps of different substrates. The unit is µm.

3.1.3 Microstructure and surface composition

3.1.3.1 *Zinc coating (Z)*

The conventional hot dip galvanized zinc coating (Z) has a uniform outermost surface chemistry with a continuous Al_2O_3 layer that covers the metallic zinc[39–42]. The surface chemistry of standard hot dip galvanized steel (Z) has been meticulously studied in the past decades, and detailed investigations about the surface chemistry, surface morphology and topography can be found in the literature[2,3,36,37,39,42–45]. In short, the surface hydrophobicity of a Z coating is explained by the thin inert Al_2O_3 layer[39]. The thickness of the alumina layer is a few nm and its presence cannot be discerned from SEM images or EDS element analysis. SEM image of the Z surface is shown in Fig. 4. After alkaline cleaning the homogeneous Al_2O_3 layer is disrupted, and the surface Al_2O_3 layer is replaced by a more reactive ZnO layer (Fig. 5). Removal of the superficial Al_2O_3 layer and formation of a secondary zinc oxide/hydroxide layer are the primary reasons for the decreased water contact angle on a Z surface as a result of alkaline cleaning (Fig 1).

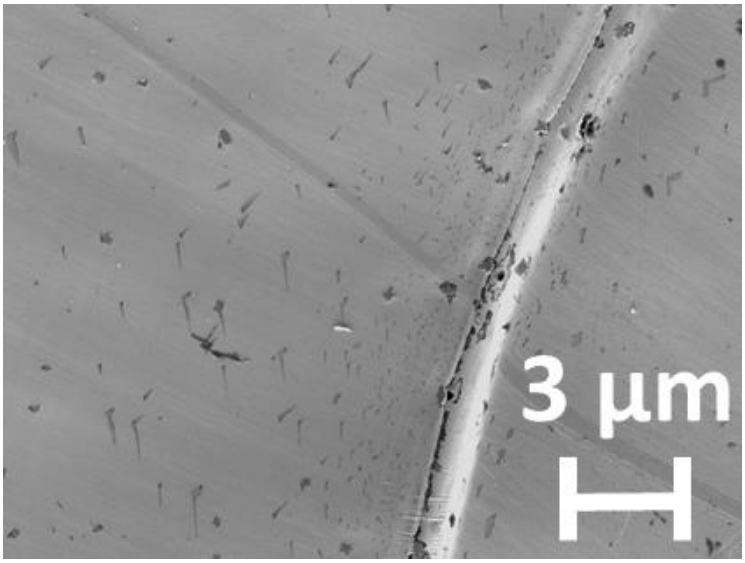

Figure 4. SEM image of an untreated Z surface with a grain boundary.

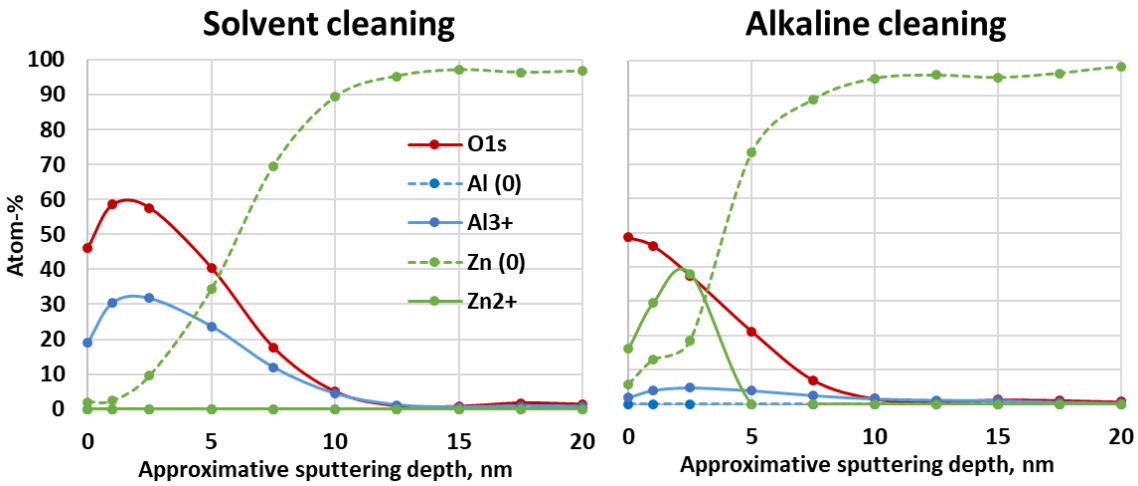

Figure 5. XPS depth profiles of Z specimens after solvent cleaning and alkaline cleaning.

3.1.3.2 *Zinc-aluminum-magnesium coating (ZMA)*

The features on the ZMA coating, i.e. Zn, Al and Mg rich phases, are very small and numerous compared to other galvanized coatings (Fig. 6). With alloying metals other than zinc, Zn grain size is reduced and the amount of eutectics is increased[6]. When Mg is added, eutectics form mainly along the grain boundaries of Zn, and more eutectic phases appear when Mg weight ratio increases[10]. A Zn-Mg-Al (ZMA) coating consists of a primary zinc phase and binary (dominant Mg-containing phase, $MgZn_2$-Zn)[46] and ternary (fine structured phase with higher Al content) eutectic phases[47]. The enhanced corrosion resistance of Mg-containing coatings has been attributed to[10]: i) limited charge transfer at grain boundaries, ii) insulating character of Mg^{2+} to zinc compounds, and iii) stabilization of the protective corrosion products of zinc by Mg^{2+}. Moderate decrease in surface hydrophobicity was obtained by alkaline cleaning of the ZMA coating (Fig. 1). This is explained by rather similar surface chemistry after solvent cleaning and alkaline cleaning (Fig. 7). In both cases, the outermost surface is composed of a mixed oxide layer (Al, Mg and Zn oxides). The thickness of the oxide layer is diminished by alkaline cleaning, but not fully removed, resulting in similar surface composition even after the surface etching step. The presence of oxidized metals in the sub-surface layers of mixed alloys has been reported earlier[44], and is not fully clear yet, but grain boundaries and phase interfaces are known to be highly oxidized compared to surrounding areas even at greater depths[2,39,48].

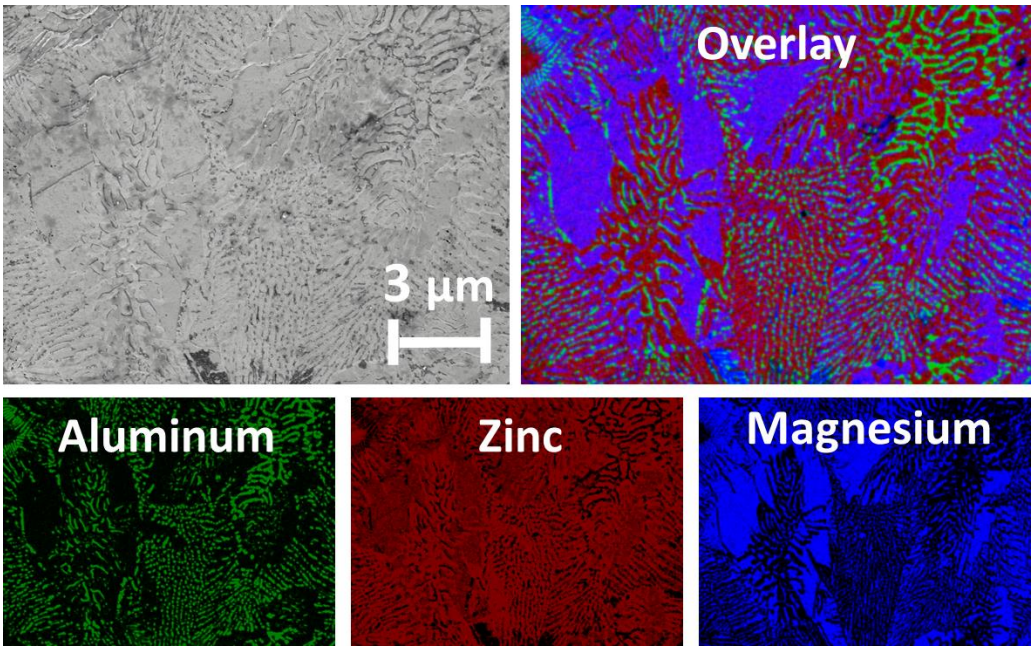

Figure 6. SEM image and EDS element maps of an untreated ZMA surface.

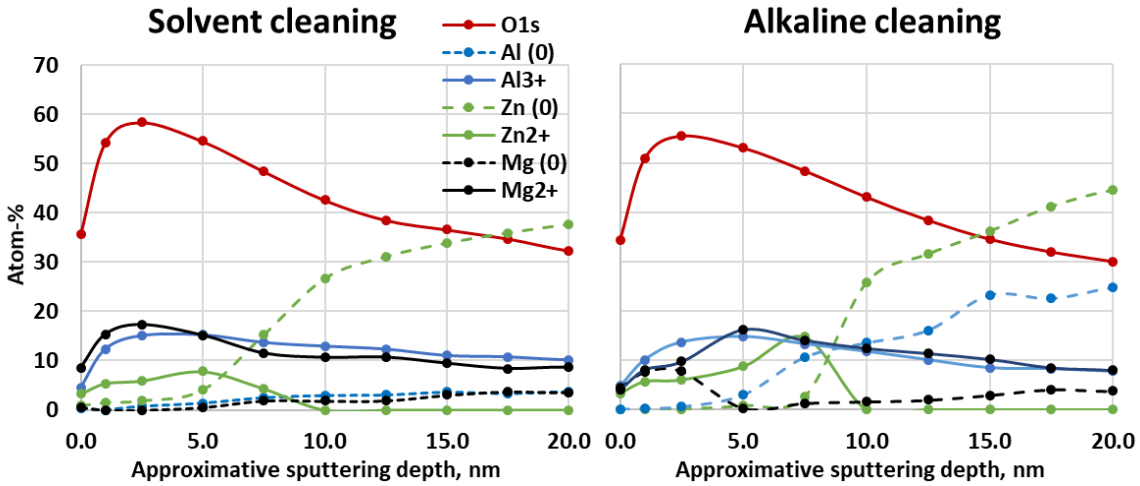

Figure 7. XPS depth profiles of ZMA specimens after solvent cleaning and alkaline cleaning.

3.1.3.3 *Galfan coating (ZA)*

Galfan coating has a surface composed of nano-sized primary γ-ZnAl, eutectic β-Zn and eutectoid α-Al+β-Zn phases[49] (Fig. 8). XPS depth profiling of the ZA coating confirmed that the outermost surface is composed of oxidized Al (Fig. 9). Considerable Al segregation on the surface has been detected for various Al-containing zinc coatings. The Al_2O_3 layer efficiently prevents zinc oxidation[44]. The XPS data shows that an oxidized aluminum layer covers all the phases (γ-ZnAl, β-Zn, and α-Al+β-Zn) on the surface of the ZA coating[44,50]. In the solvent cleaned sample, metallic zinc was present beneath the superficial alumina layer, and no traces of oxidized zinc were observed on the surface. The Al_2O_3 layer was removed by alkaline cleaning but not by solvent cleaning (Fig. 9). Removal of the Al_2O_3 layer yields similar decrease for water contact angle as for Z coating (Fig. 1).

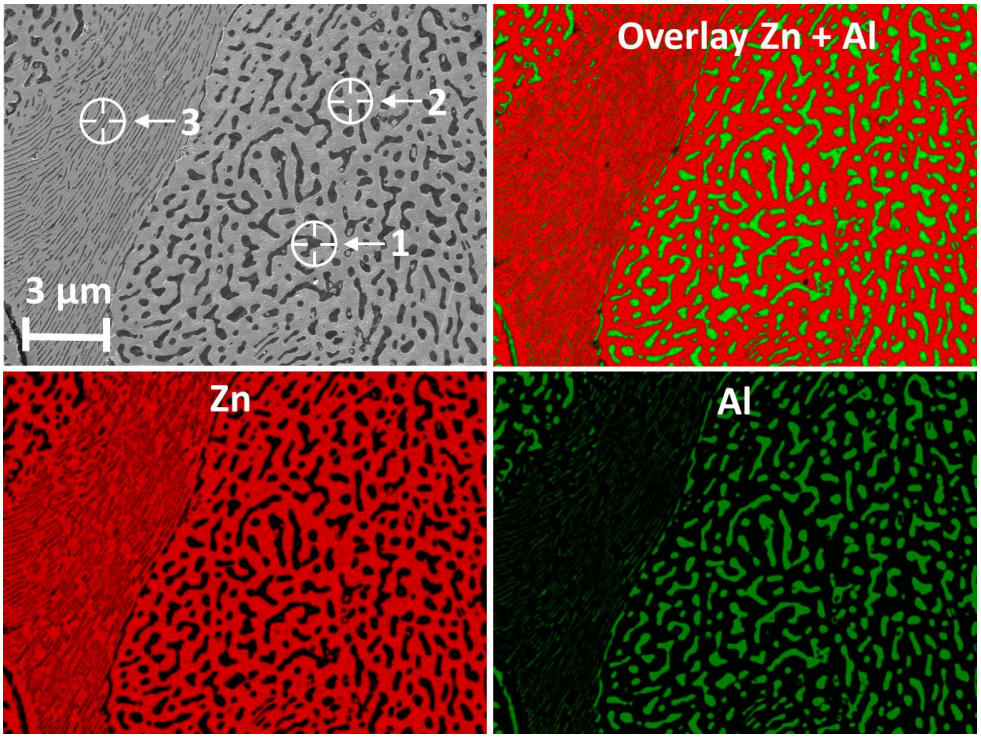

Figure 8. SEM image and EDS element maps of an untreated galfan surface. Three phases can be distinguished: 1) primary γ-ZnAl, 2) eutectic β-Zn, and 3) eutectoid α-Al+β-Zn[49].

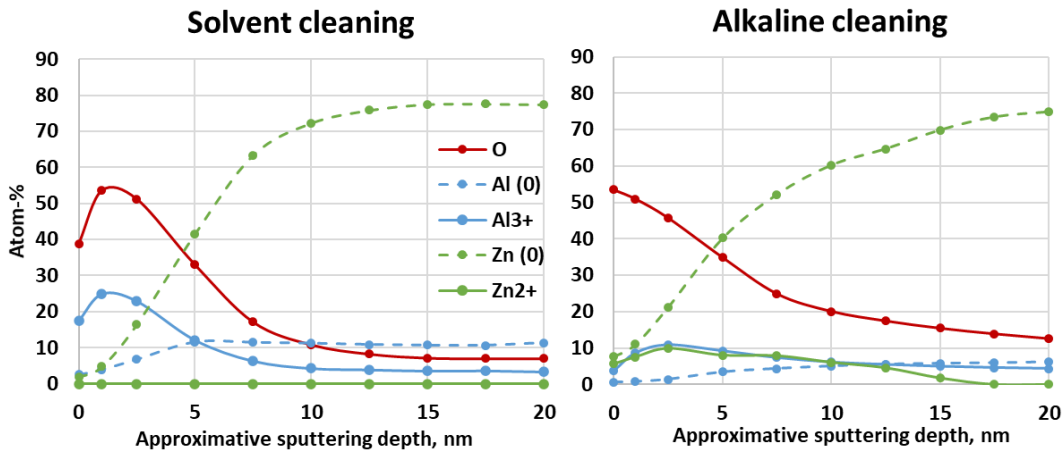

Figure 9. XPS depth profiles of ZA specimens after solvent cleaning and alkaline cleaning.

3.1.3.4 *Electrogalvanized coating (EZ)*

The outermost surface of an electrogalvanized coating is composed of small hexagonal zinc crystals that have a pyramidal morphology[18,51] (Fig. 10). The surface of the EZ coating is composed of zinc oxide, and the surface composition is not affected by alkaline cleaning (Fig. 11). Tailing of O and Zn^{2+} signals in the XPS depth profiles is most probably explained by the fine crystal topography (the surface oxide layer is not uniformly removed by XPS sputtering due to the microscopic topography variations). The decrease of water contact angle due to alkaline cleaning is moderate compared to the Al_2O_3-containing Z and ZA coatings (Fig. 1). The outermost surface of the solvent cleaned sample is composed of a slowly-formed native zinc oxide and zinc hydroxy carbonate layer[52], which cannot be discerned by molecular spectroscopy due to a very low film thickness. During alkaline cleaning this primary oxide layer is partially etched off and replaced by a newly formed, secondary zinc oxide/hydroxide layer.

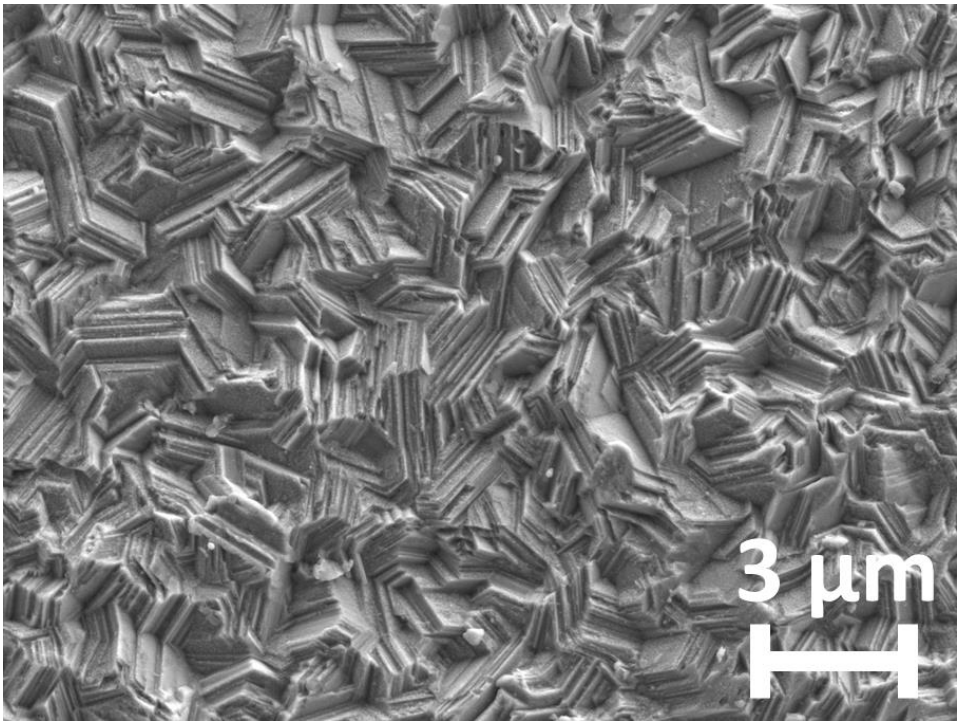

Figure 10. SEM image of an untreated EZ coating surface.

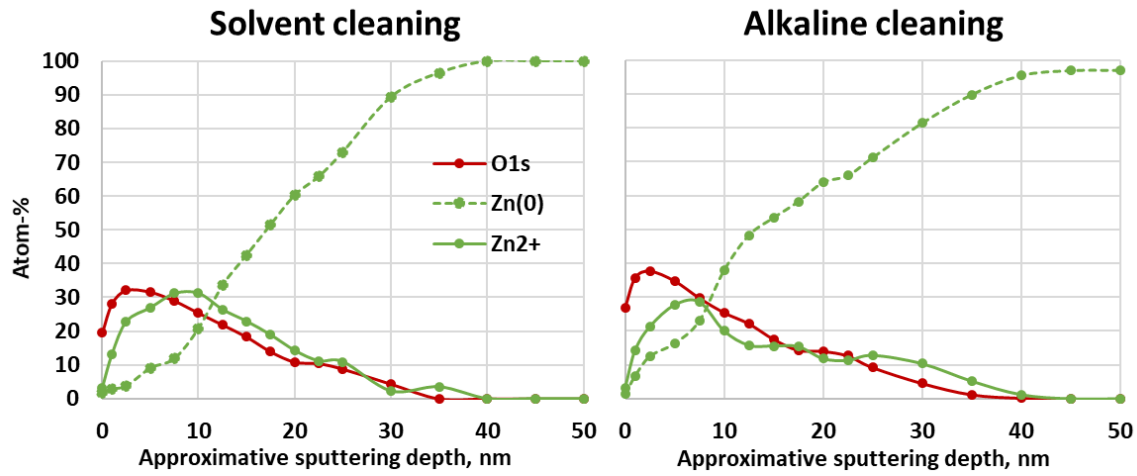

Figure 11. XPS depth profiles of EZ specimens after solvent cleaning and alkaline cleaning.

3.1.3.5 *Galvanneal coating (ZF)*

A galvanneal coating is produced by heat treatment of a hot dip galvanized coating, resulting in diffusion of iron into the zinc layer to an approximately 10 µm zinc/iron layers system[2,53]. The galvanneal coating had the roughest surface of the studied samples (Fig. 2). The coating is composed of zeta (ζ), delta (δ) and gamma (γ) intermetallic phases, including mixed phases; rod crystals pertaining to zeta phase and columnar crystals to delta phase[18,54,55]. The SEM image in Fig. 12 shows the highly porous surface of the ZF specimen. A crack is seen in the middle of the SEM image. The cracks have been attributed to stresses generated during the annealing stage and they can stretch all the way through the coating[54]. Corresponding element maps show high Al intensities scattered across the measured area, and rather even Fe distribution (Fig. 12). The high Al content is attributed to diffusion toward the free surface accelerated by the heat treatment[42,56]. According to the literature[55], the Fe content within the zinc/iron layer is approximately 10 atom-%. The EDS analysis depth with the used SEM accelerating voltage in this study, 3 kV, was about 100 nm. XPS depth profiling showed absence of iron in the outermost layer (Fig. 13). The solvent cleaned surface had a thick oxide layer composed of Al and Zn oxides. The thickness of zinc oxide layer was decreased to a couple of nm by alkaline cleaning. A strong Al^{3+} intensity confirmed that the Al_2O_3 compounds were still present. Al was not associated with Al/Fe intermetallic compounds, since metallic Al was not detected on the surface. A surface sensitive element mapping by ToF-SIMS confirmed that the very outermost ZF surface (few nm) contained very little Fe with no site-specific presence (Fig. 14). Absence of Fe on the surface of ZF coating was observed also by Feliu et al.[44] Strong Al intensity was obtained at the rough areas, while Zn dominated the flat (temper rolled) areas[44].

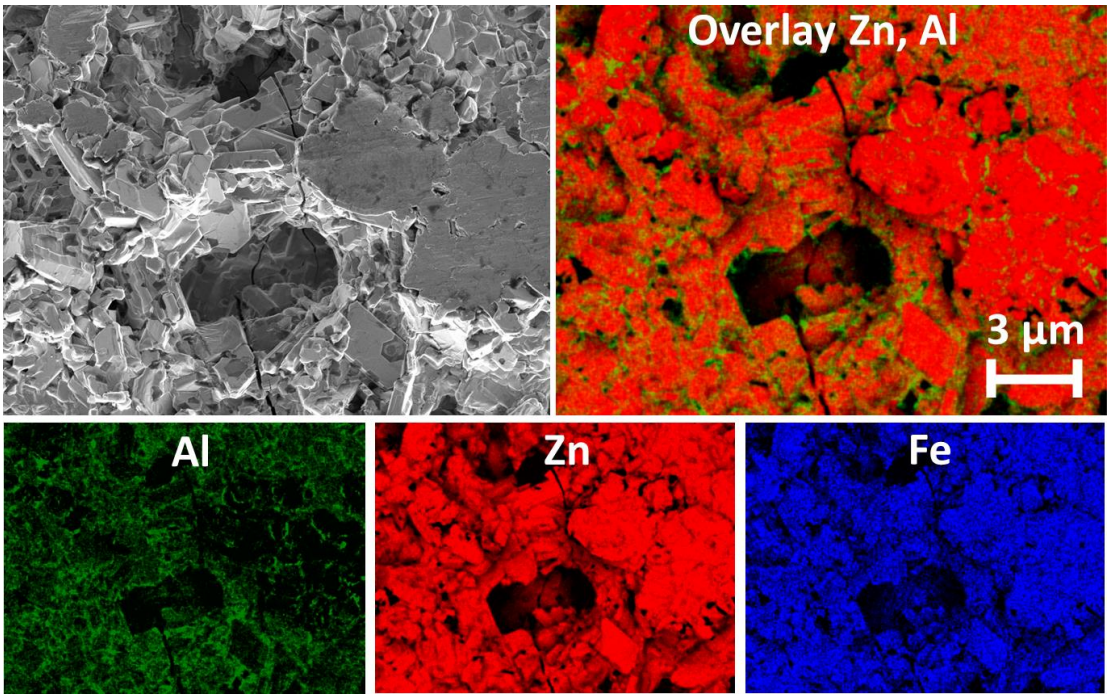

Figure 12. SEM image and EDS element maps of an untreated ZF coating. A crack in the coating is seen in the middle of the images.

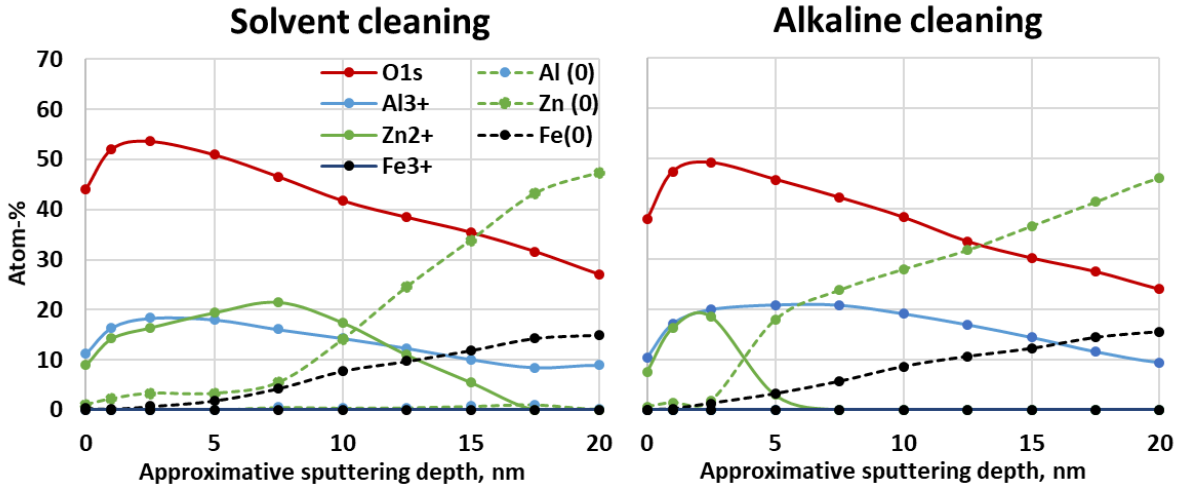

Figure 13. XPS depth profiles of ZF specimens after solvent cleaning and alkaline cleaning.

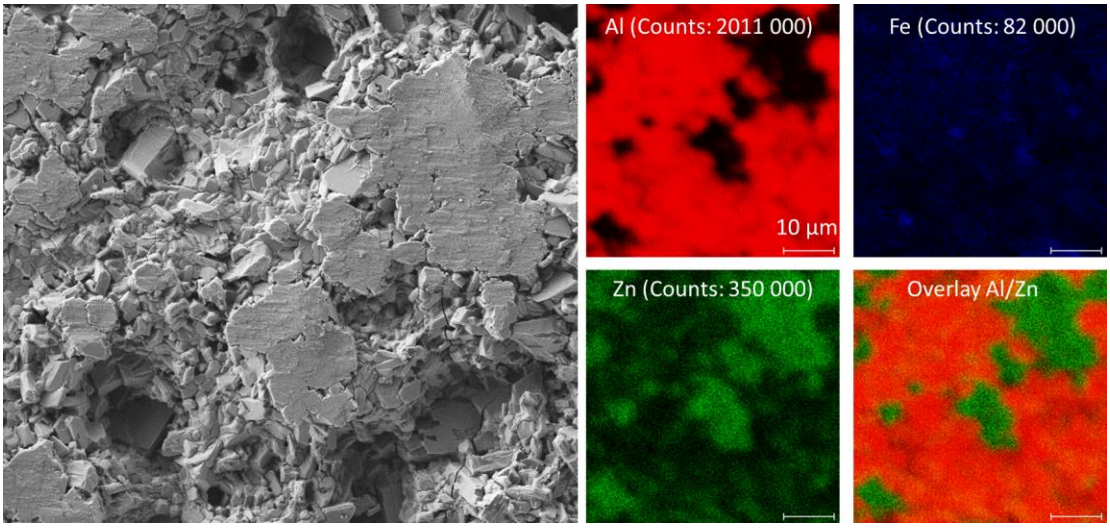

Figure 14. SEM image and corresponding ToF-SIMS element maps recorded on a ZF surface.

3.2 Characterization of samples after wet $scCO_2$ exposure

3.2.1 Characterization of corrosion products

All the samples showed FTIR spectra corresponding to hydrozincite-type corrosion products that are typically formed in outdoor exposure and have been also observed to form in wet $scCO_2$ exposure[28,33,57] (Fig. 15). The bands at 1520 and 1380 cm^{-1} arise from the v_3 symmetric stretching mode of CO_3^{2-}, and the band at 1078 cm^{-1} corresponds to the v_1 symmetric stretching mode[58,59]. Also, the v_2 bending mode of CO_3^{2-} at 835 cm^{-1} was present[59,60]. A broad band at about 470 cm^{-1} was also present, showing presence of zinc oxide[34]. The presence of zinc oxide could be attributed to intermediate corrosion products of zinc that are not fully converted to carbonates yet[11,31,33,45,61]. Unexposed zinc alloys did not yield a ZnO band (result not shown) due to a very thin oxide layer (below detection limit of the FTIR instrument), which confirms that the ZnO signal is not derived from the specimen surface but from the corrosion products formed during exposure. The signal intensity was stronger for the smooth and bright coatings (Z, ZA and EZ). Some signal background noise was seen in the spectra of ZMA and ZF coatings. This is due to increased diffuse scattering of IR-light for dull and rough surfaces (ZMA and ZF, respectively)[62]. Confirmation of magnesium corrosion products is difficult because of their similarity to crystal structure of corresponding zinc compounds[11].

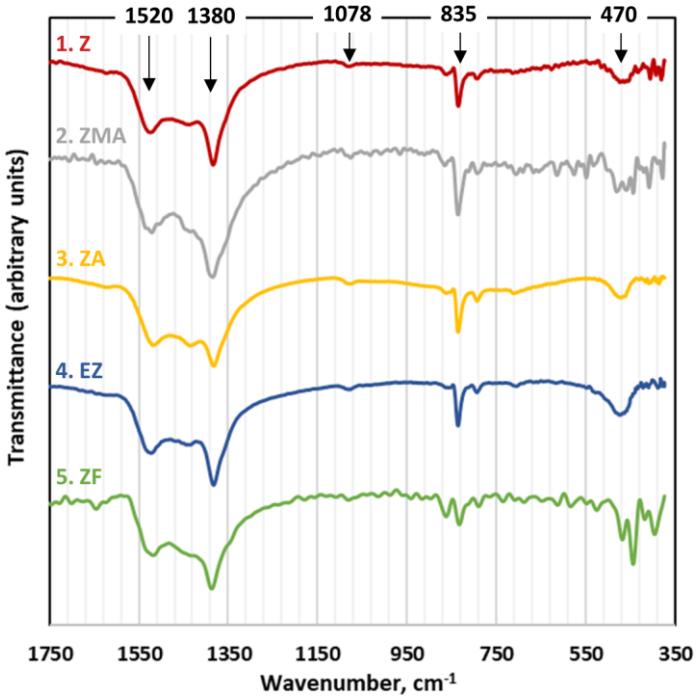

Figure 15. FTIR spectra of the specimens (alkaline cleaned) after wet $scCO_2$ exposure.

3.2.2 SEM imaging of $scCO_2$-exposed samples (alkaline-cleaned samples)

3.2.2.1 Z, ZA and EZ coatings

Local corrosion product formation was observed on the coatings, which is typical for systems with a water-saturated CO_2 phase[63] (Fig. 16). The corrosion products were precipitated as fine, grouped needle-like structures[11]. Similar structures have been observed in previous investigations in wet $scCO_2$[29,33]. Investigation of the SEM micrographs in Fig. 16 shows that the needles are more evenly distributed and smaller in size on EZ coating than on Z and ZA coatings. This indicates that the needle growth sites are more frequent on EZ coating. The pyramidal structure of the EZ surface exposes a larger reactive surface area, and more importantly, the ratio of less dense planes compared to dense planes is higher than for a hot dip galvanized zinc coating, which increases the reactivity remarkably[38,51].

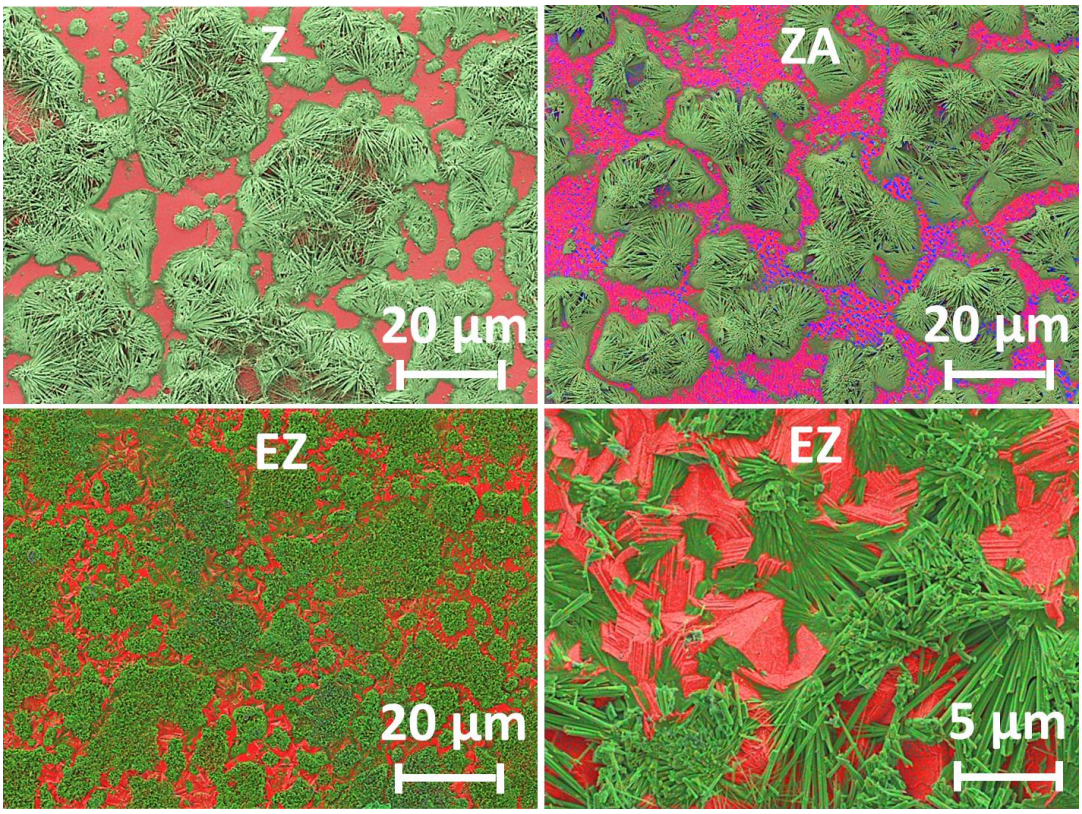

Figure 16. Wet $scCO_2$-induced corrosion products on Z, ZA and EZ surfaces. The images are overlay maps of zinc (red), aluminum (blue) and oxygen (green).

3.2.2.2 *Zinc-magnesium-aluminum coating (ZMA)*

Figures 17 and 18 show details of a wet $scCO_2$-exposed ZMA coating. The surface is partially covered with grouped needle-like corrosion products and small corrosion product particles scattered across the surface[11]. The region in the cross-section image is comprised of three micro-phases: a Zn-rich phase, Al-rich phase and Zn-Mg phase (Fig. 18). It is visible from both surface and cross section images that the Zn-Mg eutectic phase is selectively dissolved, leaving the other phases seemingly intact[10,11,57]. The corrosion product precipitation is preceded by formation of a vacant space in the alloy left by metal diffusion outwards[30]. This is proposed to occur as a result of galvanic coupling between the Zn phases and the Zn-Mg phases[46]. Zn phases are more noble than the Zn-Mg phases. Thus, the Zn phases act as local cathodes supporting reduction of dissolved oxygen and hydrogen evolution[1,64], leading to a pH increase in a close proximity to the surface and establishing a pH gradient between the anode and the cathode[46,47]. The Zn-Mg phases act as local anodes resulting to preferential dissolution of this phase. These observations show resemblance to salt-induced corrosion of ZMA coatings, where corrosion has been shown to initiate at the eutectic regions and specifically in the $MgZn_2$ lamellae, which leads to de-alloying of both the binary and ternary eutectic phases[47,65].

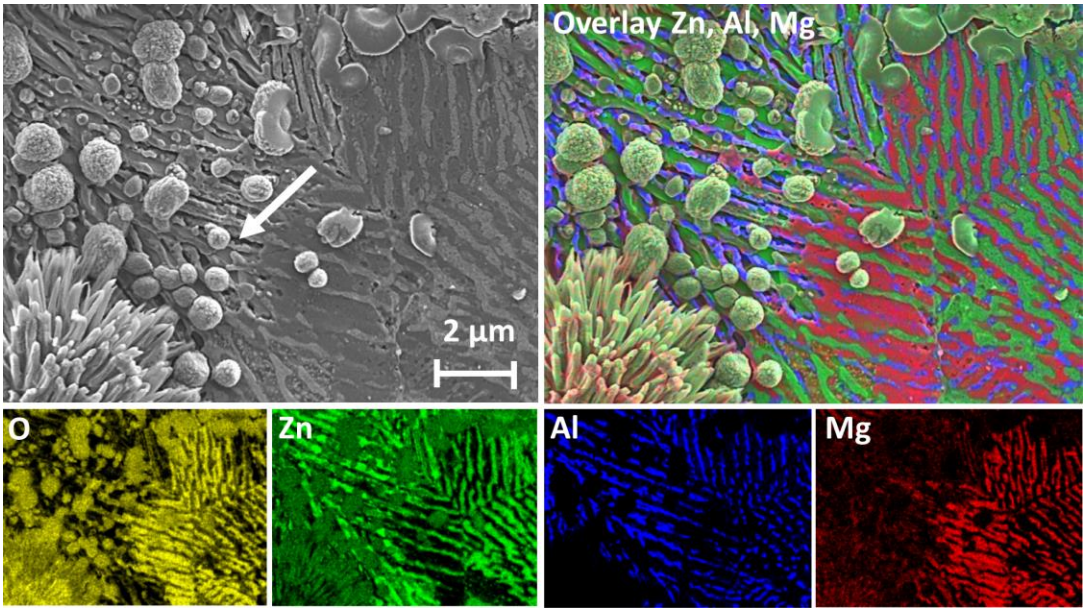

Figure 17. EDS element maps measured from the ZMA specimen after $scCO_2$ exposure. The arrow points out selective dissolution of a Zn-Mg phase.

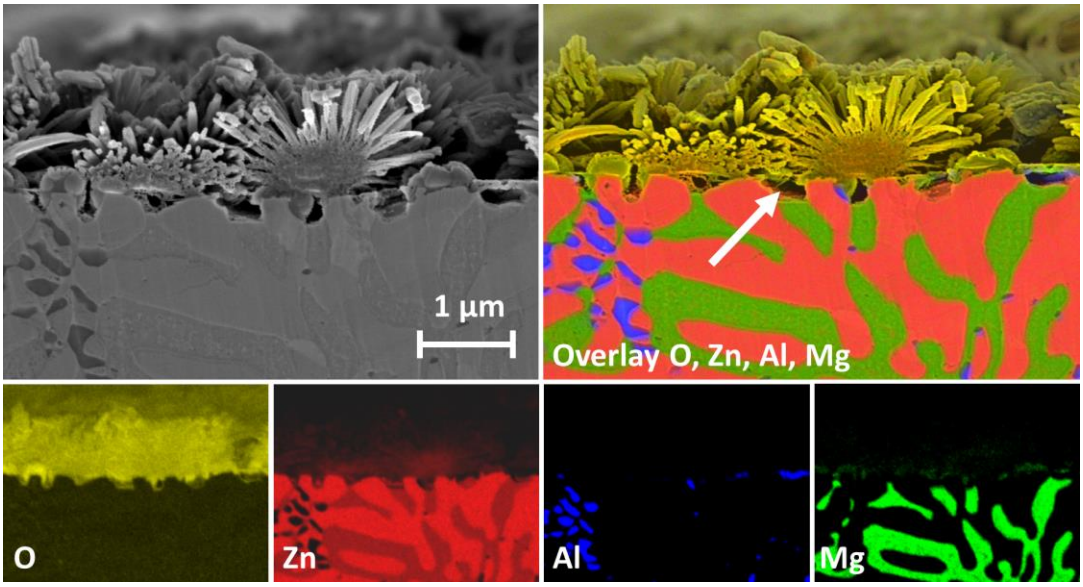

Figure 18. EDS element maps measured from a cross section of a ZMA specimen after $scCO_2$ exposure. The arrow points out selective dissolution of a Zn-Mg phase, leaving a vacant space under the precipitated corrosion products.

3.2.2.3 *Galvanneal coating (ZF)*

Needle-like corrosion products were observed primarily in the rough areas of the ZF coating (Fig. 19). In galvanized steel, the steel is protected by a zinc layer that acts as a sacrificial anode while steel acts as a cathode[1]. On the very top of the ZF coating, as was shown by XPS and ToF-SIMS measurements (Figures 13 and 14), no iron is exposed to the wet $scCO_2$ and galvanic corrosion is not the primary driver to Zn oxidization during the early-stage exposure of the coating. However, the extremely high roughness of the ZF surface, with cracks that penetrate deep into the coating, brings several intermetallic phases into contact with the wet $scCO_2$ phase simultaneously[54]. Thus, the outermost flat, Zn-rich areas are not preferentially corroded since galvanic corrosion is more prone to take place in the cavities where Fe is in close proximity to Zn. This is shown in Fig. 20, which illustrates a detail from the bottom of a rough section in the ZF coating (close to steel). A thin layer of Zn corrosion products, with small needles visible on the upper left corner of the SEM image, populates the surface of the zinc coating. The cross section confirms that several intermetallic phases are indeed susceptible to corrosion at the same time[54]. The very thin cracks (created by the stresses generated during the

annealing stage)[54] in the coating are filled with wet $scCO_2$-induced corrosion products, as shown in the EDS element maps. The crack on the right-hand side extends a few µm to the steel core and is similarly fully filled with the Zn corrosion products. This confirms galvanic corrosion as an important corrosion mechanism in wet $scCO_2$ medium. On the other hand, controlled zinc oxidation in $scCO_2$ medium, and filling of cracks by zinc corrosion products, after the annealing stage, could be a feasible step to prevent further galvanic corrosion of ZF products in the end use environment.

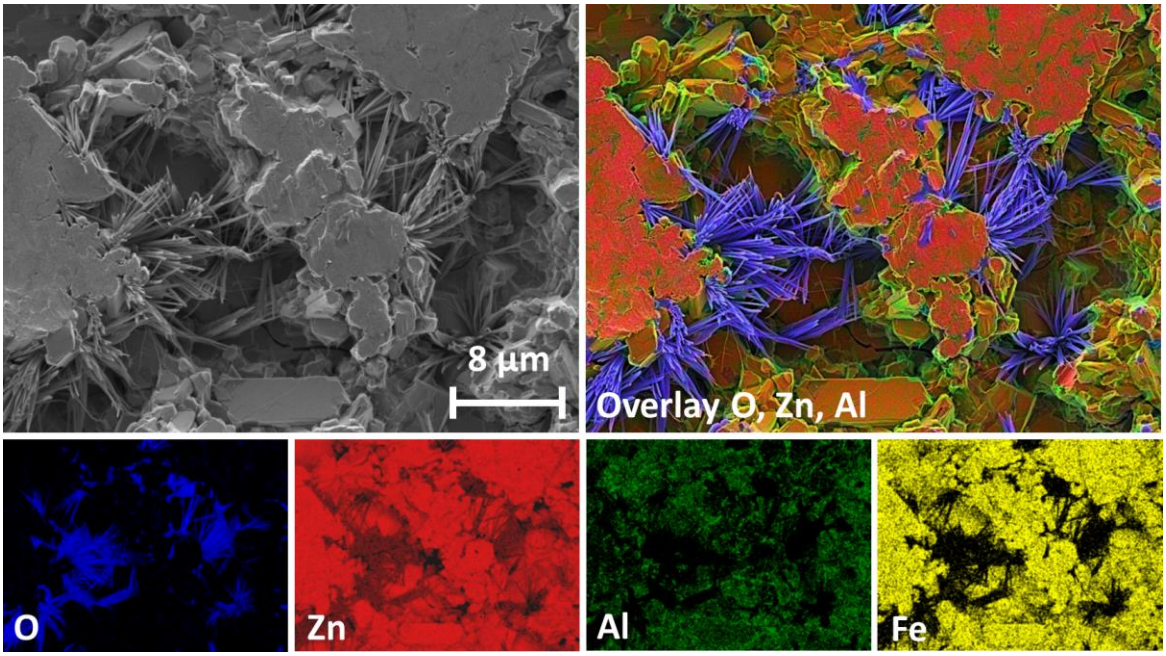

Figure 19. EDS element maps measured from the galvanneal specimen (ZF) after wet $scCO_2$ exposure.

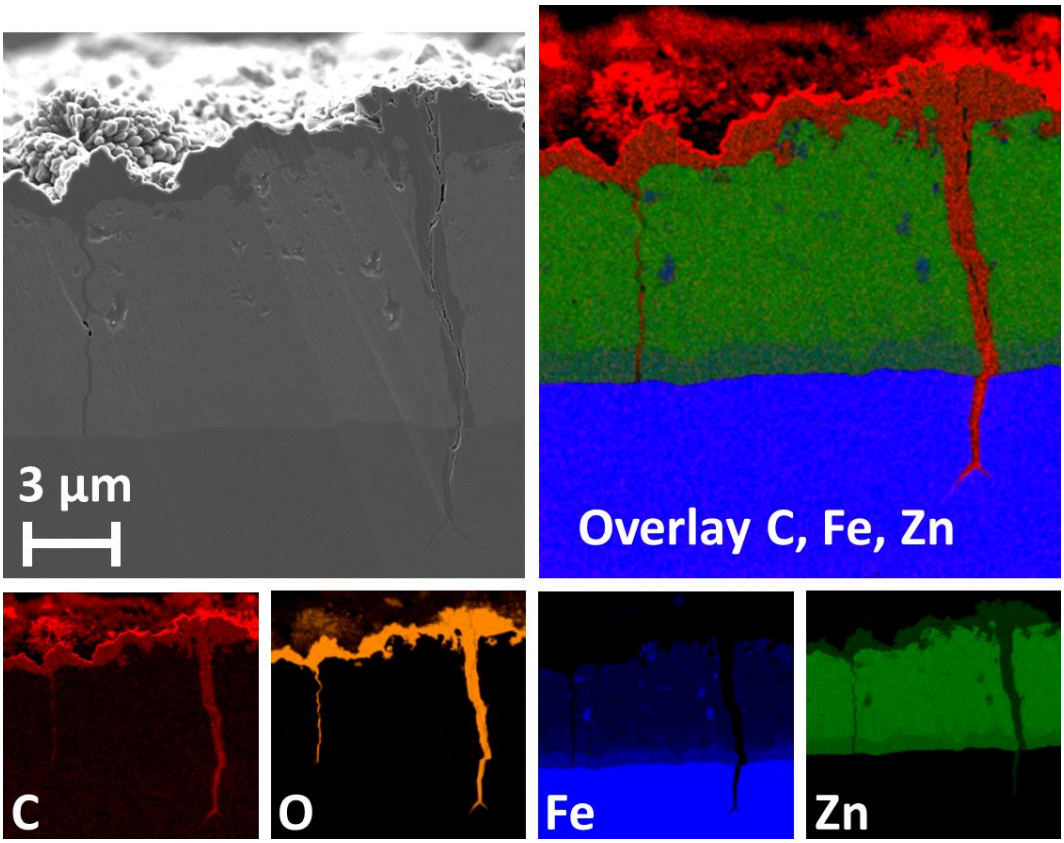

Figure 20. EDS element maps measured from a cross section of the galvanneal specimen (ZF) after $scCO_2$ exposure. C and O are the trace elements for the wet $scCO_2$-induced Zn corrosion products.

3.2.3 Quantification of corrosion products

Amount of metal ions in the extracted corrosion products is shown in Fig. 21. Corrosion product formation was scarce in solvent cleaned Z and ZA samples but increased dramatically when alkaline cleaning was employed before wet $scCO_2$ exposure. This is explained by the inert Al_2O_3 layer that reduces the reactivity of the samples (Figures 5 and 9)[3,41]. The protective nature of Al is supported by the literature, where Zn has shown selective dissolution at acidic pH (wet $scCO_2$ atmosphere), while Al has scarce solubility in the same environment[66]. After removal of the Al_2O_3 layer by alkaline cleaning, similar amount of corrosion products was formed on both Z and ZA surfaces. It should be noted that in corrosion testing the long-term zinc dissolution rate has been shown to be slower for ZA alloy due to slower electrochemical activity[3]. However, in wet $scCO_2$ exposure the early-stage corrosion product formation follows similar kinetics for these alloys. The electrogalvanized material showed very abundant corrosion product formation, which is related to absence of alloying elements other than zinc and a uniform zinc oxide layer on the finely structured pyramidal surface (with exposed, less dense and highly reactive planes)[67,68]. Zinc oxide is considered as an early intermediate compound in the reaction path for more complex zinc corrosion products[1,52,67,69]. Electrogalvanized zinc coating lacks the protective surface alumina layer, and should be carefully protected in corrosive environments[70]. Presence of a ZnO layer gives a positive electrochemical potential to the Zn surface that inherently has a negative potential, increasing ΔE, facilitating oxygen reduction and locally forming galvanic cells on metal surface[69]. Alkaline cleaning had a minimal effect on formation of zinc hydroxy carbonates on EZ substrate, since the surface was very active even without alkaline cleaning. The reactivity of ZMA and ZF alloys does not increase as much as the reactivity of Z and ZA alloys as a result of alkaline cleaning (Fig. 21). The Al_2O_3 layer was the primary factor decreasing the reactivity in the specimens in this study and presence of Mg disrupted the formation of the outermost inert alumina layer. The ZMA coating is initially (without alkaline cleaning) more prone to corrosion than standard zinc coating. Similar behavior has been reported also in alkaline environment[10]. The decreased early-stage corrosion resistance is because Zn-Mg intermetallics are more active in galvanic series than pure zinc, causing preferential corrosion in the initial corrosion process[10,47]. However, the formation of corrosion products remains on a low level even after alkaline cleaning. The presence of Mg yields a negative surface potential lower than obtained with the other alloying elements[69], efficiently suppressing oxygen reduction and resulting in lowest amount of corrosion products[65] (Fig. 21). Mg is electrochemically more active than Zn, leading to preferential dissolution of Mg and formation of stable magnesium hydroxide on the cathodes, which limit the oxygen reduction at the cathode and quench the general activity of the coating[12,65,71]. $Mg(OH)_2$ can be transformed to carbonates, similar to $Zn(OH)_2$. Only a very small amount of magnesium was detected in the corrosion products (Fig 21). It is well known that formation of MgO, $Mg(OH)_2$, $MgCO_3$ and magnesium hydroxycarbonate can take place in many environments[11,22,57,67,72–74]. However, also other ZMA corrosion studies have shown that the amount of Mg corrosion products is minute compared to Zn corrosion products, sometimes even below detection limit[10,57]. Nevertheless, the formation of initial Mg corrosion products has been stated to passivate the surface and prevent further corrosion[22]. The corrosion products on ZF substrate were solely composed of Zn-containing compounds. The corrosion products on ZF originate thus in sacrificial zinc oxidization, which is in accordance with the literature[54]. The amount of corrosion products was very high for the ZF coating. This is related to the extremely high roughness of the ZF coating compared to other coatings (Fig. 2). The roughness created by the heat treatment renders several intermetallic layers susceptible to corrosion simultaneously.

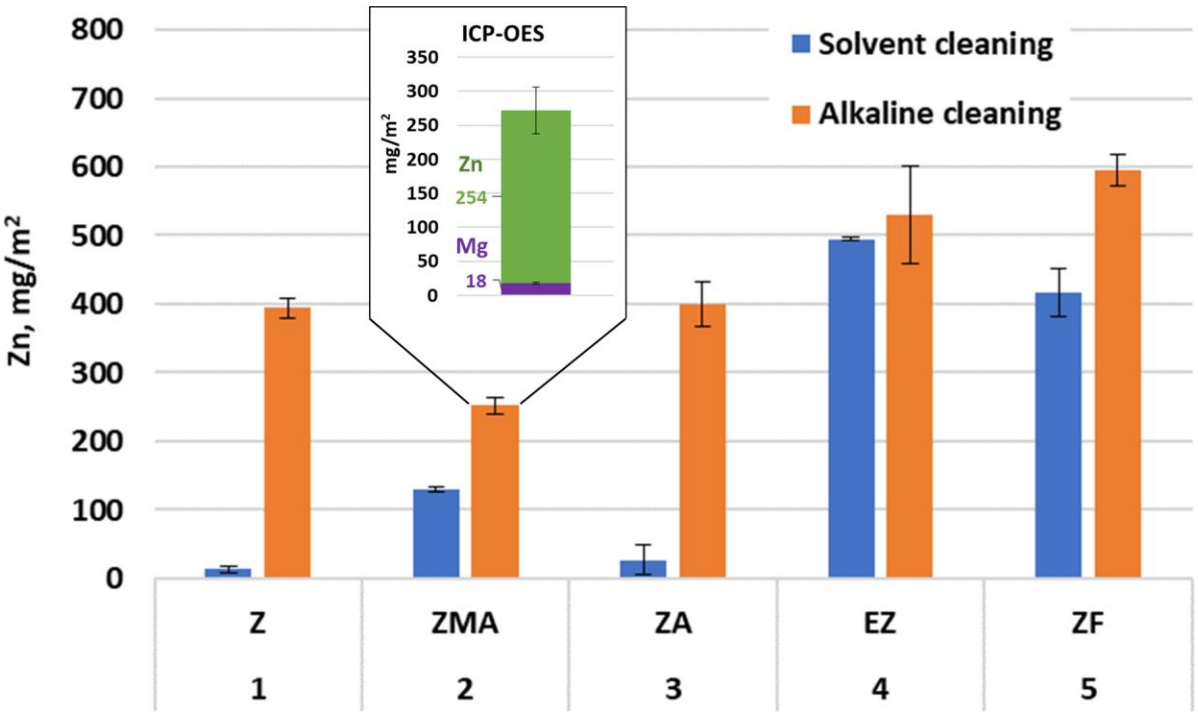

Figure 21. Quantification of Zn and Mg in glycine-extracted corrosion products.

4 CONCLUSIONS

In this study, the early-stage behavior of different zinc alloys in a wet $scCO_2$ environment was investigated. The studied coatings were zinc (Z), zinc-aluminum-magnesium (ZMA), zinc-aluminum (galfan, ZA), electrogalvanized zinc (EZ) and zinc-iron (galvanneal, ZF).

- Formation of carbonate corrosion products is much faster in supercritical carbon dioxide than in atmospheric corrosion (due to higher CO_2 concentration)
- Wet $scCO_2$ induced growth of needle-like crystals composed of zinc hydroxy carbonate on all coatings.
- On zinc (Z) and zinc-aluminum (ZA) coatings, the Al_2O_3 layer on the very outermost surface efficiently suppressed zinc oxidization.
- Alkaline cleaning activated the surface of coatings that had a superficial Al_2O_3 layer.
- An electrogalvanized coating (pure zinc) was very reactive from the beginning due to a high density of corrosion initiation points.
- The zinc-aluminum-magnesium coating was initially more reactive than Z or ZA coatings, but lower overall corrosion was observed.
- The galvanneal coating (zinc-iron coating) showed very high reactivity. The galvanneal coating has inherently a very high surface roughness with several Zn-Fe intermetallic phases exposed simultaneously to the corrosive environment. When a phase

containing Fe and Zn came to contact with the wet $scCO_2$ medium, sacrificial properties of Zn initiated growth of Zn-containing corrosion products.

- Surface chemistry had a more profound effect on corrosion product formation than the roughness. The outermost coating surface chemistry can be very different from the bulk properties of the coating and has a profound effect on initiation of the corrosion processes.

5 REFERENCES

1. Zhang, X.G., *Corrosion and Electrochemistry of Zinc*, 1st ed. (New York: Springer Science+Business Media, LCC, 1996).
2. Marder, A.R., *Prog. Mater. Sci.* 45 (2000): pp. 191–271, http://www.sciencedirect.com/science/article/pii/S0079642598000061.
3. Maeda, S., *Prog. Org. Coatings* 28 (1996): pp. 227–238.
4. Apelian, D., M. Paliwal, and D.C. Herrschaft, *Phys. Mech. Metall.* 33 (1981): pp. 12–20.
5. Bluni, S.T., A.R. Marder, and J.I. Goldstein, *Mater. Charact.* 97 (1994): pp. 93–97.
6. Yao, C., H. Lv, T. Zhu, W. Zheng, X. Yuan, and W. Gao, *J. Alloys Compd.* 670 (2016): pp. 239–248, http://dx.doi.org/10.1016/j.jallcom.2016.02.026.
7. Feliu Jr, S., and M.L. Pérez-Revenga, *Acta Mater.* 53 (2005): pp. 2857–2866.
8. Seré, P.R., C. Deyá, C.I. Elsner, and A.R. Di Sarli, *Procedia Mater. Sci.* 8 (2015): pp. 1–10, http://dx.doi.org/10.1016/j.mspro.2015.04.042.
9. Cook, D.C., R.S. Tuszynski, and H.E. Townsend, *Hyperfine Interact.* 54 (1990): pp. 781–786.
10. Wang, Y., G. Kong, C. Che, T. Weng, and Z. wen Sun, *Corros. Sci.* 136 (2018): pp. 374–385, https://doi.org/10.1016/j.corsci.2018.03.032.
11. Keppert, T.A., G. Luckeneder, K.H. Stellnberger, C. Commenda, G. Mori, and H. Antrekowitsch, *Mater. Corros.* 65 (2014): pp. 871–880.
12. Diler, E., B. Rouvellou, S. Rioual, B. Lescop, G.N. Vien, and D. Thierry, *Corros. Sci.* 87 (2014): pp. 111–117, http://dx.doi.org/10.1016/j.corsci.2014.06.017.
13. Persson, D., D. Thierry, and O. Karsson, *Corros. Sci.* 126 (2017): pp. 152–165.
14. Duchoslav, J., M. Arndt, T. Keppert, G. Luckeneder, and D. Stifter, *Anal. Bioanal. Chem.* 405 (2013): pp. 7133–7144.
15. Penney, D.J., J.H. Sullivan, and D.A. Worsley, *Corros. Sci.* 49 (2007): pp. 1321–1339.
16. Odnevall, I., and C. Leygraf, *ASTM Spec. Tech. Publ.* 1239 (1995): pp. 215–229.
17. Mokaddem, M., P. Volovitch, and K. Ogle, *Electrochim. Acta* 55 (2010): pp. 7867–7875.
18. Alvarenga, E.D.A., V. De Freitas, and C. Lins, *Surf. Coat. Technol.* 306 (2016): pp. 428–438, http://dx.doi.org/10.1016/j.surfcoat.2016.04.021.
19. Thierry, D., D. Persson, G. Luckeneder, and K.-H. Stellnberger, *Corros. Sci.* 143 (2019): pp. 338–354.
20. Huttunen-Saarivirta, E., V.E. Yudin, L.A. Myagkova, and V.M. Svetlichnyi, *Prog. Org. Coatings* 72

(2011): pp. 269–278, http://dx.doi.org/10.1016/j.porgcoat.2011.04.015.

21. Nanna, M.E., and G.P. Bierwagen, *J. Coatings Technol. Res.* 1 (2004): pp. 69–80.

22. Diler, E., B. Lescop, S. Rioual, G. Nguyen Vien, D. Thierry, and B. Rouvellou, *Corros. Sci.* 79 (2014): pp. 83–88, http://dx.doi.org/10.1016/j.corsci.2013.10.029.

23. Duarte, R.G., A.S. Castela, and M.G.S. Ferreira, *Prog. Org. Coatings* 59 (2007): pp. 206–213.

24. Carbucicchio, M., R. Ciprian, F. Ospitali, and G. Palombarini, *Corros. Sci.* 50 (2008): pp. 2605–2613.

25. Yoo, J.D., K. Ogle, and P. Volovitch, *Corros. Sci.* 81 (2014): pp. 11–20, http://dx.doi.org/10.1016/j.corsci.2013.11.045.

26. Yoo, J.D., K. Ogle, and P. Volovitch, *Corros. Sci.* 83 (2014): pp. 32–37, http://dx.doi.org/10.1016/j.corsci.2013.12.024.

27. Latosov, E., B. Maaten, A. Siirde, and A. Konist, *Energy Procedia* 147 (2020): pp. 63–70, https://doi.org/10.1016/j.egypro.2018.07.034.

28. Falk, T., J. Svensson, and L. Johansson, *J. Electrochem. Soc.* 145 (1998): pp. 39–44.

29. Saarimaa, V., A. Kaleva, J.-P. Nikkanen, J. Manni, C. Lange, T. Paunikallio, T. Laihinen, S. Heinonen, E. Levänen, P. Väisänen, and A. Markkula, *ACS Appl. Mater. Interfaces* 10 (2018): pp. 21730–21739.

30. Sarrade, S., D. Féron, F. Rouillard, S. Perrin, R. Robin, J.C. Ruiz, and H.A. Turc, *J. Supercrit. Fluids* 120 (2017): pp. 335–344, http://dx.doi.org/10.1016/j.supflu.2016.07.022.

31. Kaleva, A., T. Tassaing, V. Saarimaa, G. Le Bourdon, P. Väisänen, A. Markkula, and E. Levänen, *Corros. Sci.* 174 (2020), https://doi.org/10.1016/j.corsci.2020.108850.

32. Saarimaa, V., A. Kaleva, J.P. Nikkanen, S. Heinonen, E. Levänen, P. Väisänen, A. Markkula, and J. Juhanoja, *Surf. Coatings Technol.* 331 (2017): pp. 137–142, http://dx.doi.org/10.1016/j.surfcoat.2017.10.047.

33. Kaleva, A., V. Saarimaa, S. Heinonen, J.-P. Nikkanen, A. Markkula, P. Väisänen, and E. Levänen, *Nanomaterials* 7 (2017): pp. 181–190, http://www.mdpi.com/2079-4991/7/7/181.

34. Saarimaa, V., A. Kaleva, T. Paunikallio, J.-P. Nikkanen, S. Heinonen, E. Levänen, P. Väisänen, and A. Markkula, *Surf. Interface Anal.* 50 (2018): pp. 564–570.

35. Beccaria, A., *Corrosion* 46 (1990): pp. 906–912.

36. Berger, R., U. Bexell, N. Stavlid, and T.M. Grehk, *Surf. Interface Anal.* 38 (2006): pp. 1130–1138.

37. Hörnström, S.E., E.G. Hedlund, H. Klang, J.-O. Nilsson, M. Backlund, and P.-E. Tegehall, *Surf. Interface Anal.* 19 (1992): pp. 121–126.

38. Khorsand, S., K. Raeissi, and M.A. Golozar, *Corros. Sci.* 53 (2011): pp. 2676–2678.

39. Biber, H.E., *Metall. Trans. A* 19A (1988): pp. 1603–1608.

40. Zapponi, M., A. Quiroga, and T. Pérez, *Surf. Coatings Technol.* 122 (1999): pp. 18–20.

41. Wolpers, M., and J. Angeli, *Appl. Surf. Sci.* 179 (2001): pp. 281–291.

42. Rodnyansky, A., Y. Warburton, and L. Hanke, *Surf. Interface Anal.* 29 (2000): pp. 215–220.

43. Saarimaa, V., A. Markkula, J. Juhanoja, and B.-J. Skrifvars, *Surf. Coatings Technol.* 306 (2016).

44. Feliu Jr., S., and V. Barranco, *Acta Mater.* 51 (2003): pp. 5413–5424.

45. Leroy, V., *Mater. Sci. Eng.* 42 (1980): pp. 289–307.

46. Lostak, T., A. Maljusch, B. Klink, S. Krebs, M. Kimpel, J. Flock, S. Schulz, and W. Schuhmann, *Electrochim. Acta* 137 (2014): pp. 65–74, http://dx.doi.org/10.1016/j.electacta.2014.05.163.

47. Sullivan, J., S. Mehraban, and J. Elvins, *Corros. Sci.* 53 (2011): pp. 2208–2215, http://dx.doi.org/10.1016/j.corsci.2011.02.043.

48. Strutzenberger, J., and J. Faderl, *Met. Mater. Trans. A* 29A (1998): pp. 631–645.

49. Wei, X., L. Ren, X. Geng, Z. Sun, H. Hu, X. Nie, and A. Banerji, *Mater. Charact.* 147 (2019): pp. 295–302, https://doi.org/10.1016/j.matchar.2018.11.016.

50. Leroy, V., "Surface Properties of Zn Base Coated Steels by Hot Dipping or Electrodeposition," in Proc. Int. Conf. Zinc Zinc Alloy Coat. Steel Sheet (Tokyo: The iron and steel institute of Japan, 1989), pp. 399–409.

51. Park, H., and J.A. Szpunar, *Corros. Sci.* 40 (1998): pp. 525–545.

52. Thomas, S., N. Birbilis, M.S. Venkatraman, and I.S. Cole, *Corros. Sci.* 69 (2013): pp. 11–22, http://dx.doi.org/10.1016/j.corsci.2013.01.011.

53. Wienströer, S., M. Fransen, H. Mittelstädt, C. Nazikko, and M. Völker, *Adv. X-Ray Anal.* 46 (2003): pp. 291–296.

54. Queiroz, F.M., and I. Costa, *Surf. Coatings Technol.* 201 (2007): pp. 7024–7035.

55. Raghavan, V., *J. Phase Equilibria* 24 (2003): pp. 544–545.

56. Mataigne, J.-M., V. Vaché, and M. Repoux, *Rev. Métallurgie* 106 (2007): pp. 41–47.

57. LeBozec, N., D. Thierry, D. Persson, C.K. Riener, and G. Luckeneder, *Surf. Coatings Technol.* 374 (2019): pp. 897–909, https://doi.org/10.1016/j.surfcoat.2019.06.052.

58. Loring, J., C. Thompson, C. Zhang, Z. Wang, H. Schaef, and K. Rosso, *J. Phys. Chem. A* 116 (2012): pp. 4768–4777.

59. Hales, M.C., and R.L. Frost, *Polyhedron* 26 (2007): pp. 4955–4962.

60. Sanna, R., G. De Giudici, A.M. Scorciapino, C. Floris, and M. Casu, *Am. Miner.* 98 (2013): pp. 1219–1226.

61. Saarimaa, V., A. Kaleva, J.-P. Nikkanen, S. Heinonen, E. Levänen, P. Väisänen, A. Markkula, and J. Juhanoja, *Surf. Coatings Technol.* 331 (2017): pp. 137–142.

62. Saarimaa, V., N. Fuertes, D. Persson, T. Zavalis, A. Kaleva, J.-P. Nikkanen, E. Levänen, and G. Heydari, *Mater. Corros.* (2020).

63. Cui, G., Z. Yang, J. Liu, and Z. Li, *Int. J. Greenh. Gas Control* 90 (2019): pp. 1–17, https://doi.org/10.1016/j.ijggc.2019.102814.

64. Bastos, A.C., M.C. Quevedo, O. V. Karavai, and M.G.S. Ferreira, *J. Electrochem. Soc.* 164 (2017): pp. C973–C990.

65. Prosek, T., J. Hagström, D. Persson, N. Fuertes, F. Lindberg, O. Chocholatý, C. Taxén, J. Šerák, and D. Thierry, *Corros. Sci.* 110 (2016): pp. 71–81.

66. Vu, T.N., P. Volovitch, and K. Ogle, *Corros. Sci.* 67 (2013): pp. 42–49, http://dx.doi.org/10.1016/j.corsci.2012.09.042.

67. Volovitch, P., C. Allely, and K. Ogle, *Corros. Sci.* 51 (2009): pp. 1251–1262.

68. Zhu, L., F. Yang, and N. Ding, *Surf. Coatings Technol.* 201 (2007): pp. 7829–7834.

69. Nazarov, A., D. Thierry, T. Prosek, and N. Le Bozec, *J. Electrochem. Soc.* 152 (2005): p. B220.

70. Winiarski, J., J. Masalski, and B. Szczygie, *Surf. Coat. Technol.* 236 (2013): pp. 252–261.

71. Prestat, M., L. Holzer, B. Lescop, S. Rioual, C. Zaubitzer, E. Diler, and D. Thierry, *Electrochem. Commun.* 81 (2017): pp. 56–60.

72. Unocic, K.A., H.H. Elsentriecy, M.P. Brady, H.M. Meyer, G.L. Song, M. Fayek, R.A. Meisner, and B. Davis, *J. Electrochem. Soc.* 161 (2014): pp. C302–C311, http://jes.ecsdl.org/cgi/doi/10.1149/2.024406jes.

73. Kwak, J.H., J.Z. Hu, R.V.F. Turcu, K.M. Rosso, E.S. Ilton, C. Wang, J.A. Sears, M.H. Engelhard, A.R. Felmy, and D.W. Hoyt, *Int. J. Greenh. Gas Control* 5 (2011): pp. 1081–1092, http://dx.doi.org/10.1016/j.ijggc.2011.05.013.

74. Felmy, A.R., O. Qafoku, B.W. Arey, J.Z. Hu, M. Hu, H. Todd Schaef, E.S. Ilton, N.J. Hess, C.I. Pearce, J. Feng, and K.M. Rosso, *Geochim. Cosmochim. Acta* 91 (2012): pp. 271–282, http://dx.doi.org/10.1016/j.gca.2012.05.026.

6 FIGURE CAPTIONS

Figure 1. Water contact angles on different substrates after solvent cleaning and alkaline cleaning.

Figure 2. Roughness values of the studied substrates.

Figure 3. Confocal microscopy contour maps of different substrates. The unit is μm.

Figure 4. SEM image of an untreated Z surface with a grain boundary.

Figure 5. XPS depth profiles of Z specimens after solvent cleaning and alkaline cleaning.

Figure 6. SEM image and EDS element maps of an untreated ZMA surface.

Figure 7. XPS depth profiles of ZMA specimens after solvent cleaning and alkaline cleaning.

Figure 8. SEM image and EDS element maps of an untreated galfan surface. Three phases can be distinguished: 1) primary γ-ZnAl, 2) eutectic β-Zn, and 3) eutectoid α-Al+β-Zn[49].

Figure 9. XPS depth profiles of ZA specimens after solvent cleaning and alkaline cleaning.

Figure 10. SEM image of an untreated EZ coating surface.

Figure 11. XPS depth profiles of EZ specimens after solvent cleaning and alkaline cleaning.

Figure 12. SEM image and EDS element maps of an untreated ZF coating. A crack in the coating is seen in the middle of the images.

Figure 13. XPS depth profiles of ZF specimens after solvent cleaning and alkaline cleaning.

Figure 14. SEM image and corresponding ToF-SIMS element maps recorded on a ZF surface.

Figure 15. FTIR spectra of the specimens (alkaline cleaned) after wet $scCO_2$ exposure.

Figure 16. Wet $scCO_2$-induced corrosion products on Z, ZA and EZ surfaces. The images are overlay maps of zinc (red), aluminum (blue) and oxygen (green).

Figure 17. EDS element maps measured from the ZMA specimen after $scCO_2$ exposure. The arrow points out selective dissolution of a Zn-Mg phase.

Figure 18. EDS element maps measured from a cross section of a ZMA specimen after $scCO_2$ exposure. The arrow points out selective dissolution of a Zn-Mg phase, leaving a vacant space under the precipitated corrosion products.

Figure 19. EDS element maps measured from the galvanneal specimen (ZF) after wet $scCO_2$ exposure.

Figure 20. EDS element maps measured from a cross section of the galvanneal specimen (ZF) after

$scCO_2$ exposure. C and O are the trace elements for the wet $scCO_2$-induced Zn corrosion products.

Figure 21. Quantification of Zn and Mg in glycine-extracted corrosion products.

7 TABLES

Table 1: List of coatings.

No	Coating method	Coating name	Acronym	Coating weight, g/m^2	Coating thickness, µm	Approximative coating composition, wt-%
1	Hot dip galvanizing	Zinc	Z	275	20	0.2% Al, 99.8% Zn
2	Hot dip galvanizing	Zinc-aluminum-magnesium	ZMA	275	20	1.5% Al, 1.5% Mg, 97% Zn
3	Hot dip galvanizing	Galfan	ZA	275	20	5% Al, 95% Zn
4	Electroplating	Electrogalvanized	EZ	50	6	99.9% Zn
5	Hot dip galvanizing and heat treatment	Galvanneal	ZF	275	20	0.2% Al, ~10% Fe, ~90% Zn